Riser modal identification in CFD and full-scale experiments

D. Lucor[a], H. Mukundan[b], M.S. Triantafyllou[b],*

[a]*Laboratoire de Modélisation en Mécanique, Université Pierre et Marie Curie, 4 place Jussieu, Paris, France*
[b]*Department of Ocean Engineering, Massachusetts Institute of Technology, Cambridge, MA 02139, USA*

Abstract

A systematic methodology is presented to obtain the vortex-induced vibrational modes of a riser, based on data from CFD coupled to a long beam under tension and placed in sheared cross-flow; two profiles were tested: (a) linear, and (b) exponential. The *modes* we estimate are in fact nonlinear equilibria between the flow-induced excitation forces and the structural dynamics and are characterized by varying amplitude and phase along the span; these are *complex modes*, mixtures of traveling and standing waves. Simplifying procedures to represent the VIV response in terms of a few clusters of modes have been applied successfully, reducing substantially the data needed to represent the VIV response.
© 2006 Elsevier Ltd. All rights reserved.

1. Introduction

Vortex-induced vibrations (VIV) of bluff, flexibly mounted rigid structures and long flexible structures with bluff cross-section, placed within a transverse oncoming flow, constitute a self-excited, self-limiting process. Indeed, excitation forces are caused by an instability of the wake flow, but once the structure starts vibrating, the forces change and eventually become resistive, beyond an amplitude of vibration typically around one transverse body dimension (Sarpkaya, 1979; Zdravkovich, 1997; Govardhan and Williamson, 2000). The wake instability has a preferred frequency, the Strouhal frequency f_S; if the structural natural frequency is close to f_S, then vibrations are excited at a frequency near the natural and Strouhal frequency, as determined by the added mass of the structure, which is frequency- and amplitude-dependent. Hence, within a uniform current the spectrum of the excitation forces, as well as the spectrum of the system response, is found to have a large peak, often the only peak, within a narrow frequency range relatively close to its natural frequency (Triantafyllou et al., 2003).

In the case of a flexible structure, such as a uniform taut string, or a uniform tensioned beam, placed in a uniform current, a narrow-band response may be observed, resulting in apparently standing waves, such as one would expect from free vibrations of such structures. However, these are self-excited vibrations whose amplitude is limited by either the structural damping or the self-limiting nature of the fluid forces; hence, they can be thought of as *nonlinear dynamic equilibria* of the fluid-structure interaction process. Since they result from a resonant matching between fluid excitation and small-amplitude (hence linearizable) structural response, the nonlinearity is almost entirely due to the fluid. We will call these flow-structure interaction monochromatic, or narrow-band responses *modes*, recognizing that they may bear no resemblance to free vibration structural modes.

---

*Corresponding author. Tel.: +1 617 253 4335; fax: +1 617 253 8125.
 E-mail address: mistetri@mit.edu (M.S. Triantafyllou).

In the case of nonuniform current, the excitation is not at a single frequency, since the Strouhal frequency depends linearly on the spatially variable speed of flow (Stansby, 1976). As a result, a wide-band excitation is obtained, resulting in excitation of a single natural frequency, if the natural frequencies are spaced far apart from each other; or of several natural frequencies of the system, if densely spaced (Vandiver et al., 1996). The mechanics of multi-frequency response are largely unknown, since the parametric space is too large to explore experimentally or numerically, even at low Reynolds number.

If a single frequency is excited in a sheared current, it is expected qualitatively that energy is input at a frequency close to the local Strouhal frequency over a part of the flexible structure, and then is carried away to be dissipated at another part of the structure, where the local Strouhal frequency is different and the fluid force resists the traveling wave, providing a damping force. In such a case, the response of the structure cannot be described in the form of standing waves, which do not allow energy to be carried along the length of the structure. Semi-empirical programs, which utilize structural models combined with experimental fluid data to represent the flow–structure interaction phenomenon, predict the presence of *complex modes*, i.e. a response whose amplitude and phase varies along the length of the structure, a mixture of traveling and standing waves (Triantafyllou et al., 1999). Questions as to how the excitation/damping forcing is distributed along the length, and which frequency predominates are important for understanding the phenomenon and developing effective models for representing it (Gopalkrishnan, 1992). When a multi-frequency response is excited, several *modes* will participate, one for each frequency of excitation. Several additional questions arise: are these modes statistically stationary; do they interact strongly with each other; and do they resemble the modes of single frequency response?

To address the problem, we have conducted a modal decomposition of detailed numerical simulation data. First we employed spectral numerical simulations with no underlying turbulence model, of linear and exponential turbulent shear flows, at Reynolds numbers up to 1000, past long tensioned beams with circular cross-section. We then employed a numerical procedure, which will be described in detail, to extract these nonlinear modes and study their properties. We should point out that our turbulent flows numerical simulations are related but not identical to direct numerical simulations (DNS). By definition, DNS data can provide a very detailed description of the response as well as the hydrodynamic forces both in the spatial and temporal domains. This is particularly true for structures with short or moderately long aspect ratios (Lucor et al., 2001, 2005). Here, however, the structure is too long to meet the DNS spanwise resolution requirement. For structures with long aspect ratios, it was shown that the initial conditions, the numerical spanwise resolution and the extent of a numerical buffer region play an important role in the variability and the accuracy of the response prediction (Lucor et al., 2003).

2. Derivation of the phase reconstruction

All quantities in the following are nondimensional quantities. The data are *discrete* data in time and space. Let us consider the structural response at some particular time t_k and some particular location z_j along the span of the cylinder. Both the spatial and temporal grids have equidistant grid points. We assume that we can express the response $y(t_k, z_j)$ of the structure as

$$y(t_k, z_j) = \mathcal{R}e\left\{ \sum_{n=1}^{N} e^{i\omega_n t_k} \phi_n(z_j) \right\} = \mathcal{R}e\left\{ \sum_{n=1}^{N} e^{i2\pi nk/P}(\phi_{n_{\mathcal{R}e}}(z_j) + i\phi_{n_{\mathcal{I}m}}(z_j)) \right\}. \tag{1}$$

Here, $\omega_n = n\Omega$ is defined as the nth circular frequency sample with $\Omega = 2\pi/P\Delta T$, P is the total number of time samples and ΔT is the sampling interval. We also define the nth frequency sample $f_n = \omega_n/2\pi$. The time t_k refers to the kth time sample and $t_k = k\Delta T$. The integer n will also be referred as the nth temporal mode. The unknowns here are the real part $\phi_{n_{\mathcal{R}e}}(z_j)$ and the imaginary part $\phi_{n_{\mathcal{I}m}}(z_j)$ for each mode n and each point j in the domain. In compact form, we have

$$y(t_k, z_j) = \mathcal{R}e\left\{ \Delta_k^{\mathrm{T}} \phi_j \right\} \quad \text{with} \quad \phi_j = [\phi_1(z_j)\phi_2(z_j)\cdots\phi_N(z_j)]^{\mathrm{T}}, \quad \Delta_k = [e^{i\omega_1 t_k}e^{i\omega_2 t_k}\cdots e^{i\omega_N t_k}]^{\mathrm{T}}, \tag{2}$$

where the superscript T is the transpose operator. It follows that

$$\mathbf{y}_k = \begin{bmatrix} y(t_k, z_1) \\ \vdots \\ y(t_k, z_j) \\ \vdots \\ y(t_k, z_M) \end{bmatrix} = \mathcal{R}e\left\{ \begin{bmatrix} \Delta_k^{\mathrm{T}}\phi_1 \\ \vdots \\ \Delta_k^{\mathrm{T}}\phi_j \\ \vdots \\ \Delta_k^{\mathrm{T}}\phi_M \end{bmatrix} \right\} = \mathcal{R}e\{\hat{\Delta}_k\hat{\phi}\} \quad \text{with} \quad \hat{\Delta}_k = \begin{bmatrix} \Delta_k^{\mathrm{T}} & & \cdots & 0 \\ & \Delta_k^{\mathrm{T}} & \cdots & 0 \\ \vdots & \vdots & \ddots & \vdots \\ 0 & 0 & \cdots & \Delta_k^{\mathrm{T}} \end{bmatrix}, \quad \hat{\phi} = \begin{bmatrix} \phi_1 \\ \vdots \\ \phi_j \\ \vdots \\ \phi_M \end{bmatrix}. \tag{3}$$

Finally, we have

$$Y = [y_1 \cdots y_k \cdots y_P]^{\mathrm{T}} = \mathscr{R}e\{[\hat{\Delta}_1\ \hat{\phi} \cdots \hat{\Delta}_k \hat{\phi} \cdots \hat{\Delta}_P \hat{\phi}]^{\mathrm{T}_b}\} = \mathscr{R}e\{\Delta\}\mathscr{R}e\{\hat{\phi}\} - \mathscr{I}m\{\Delta\}\ \mathscr{I}m\{\hat{\phi}\},$$ (4)

with

$$\Delta = [\hat{\Delta}_1 \cdots \hat{\Delta}_k \cdots \hat{\Delta}_P]^{\mathrm{T}} = \begin{bmatrix} \Delta_1^{\mathrm{T}} & \cdots & \cdots & 0 & \Delta_k^{\mathrm{T}} & \cdots & \cdots & 0 & \Delta_P^{\mathrm{T}} & \cdots & \cdots & 0 \\ \vdots & \Delta_1^{\mathrm{T}} & \cdots & 0 & \vdots & \Delta_k^{\mathrm{T}} & \cdots & 0 & \vdots & \Delta_P^{\mathrm{T}} & \cdots & 0 \\ \vdots & \vdots & \ddots & \vdots & \vdots & \vdots & \ddots & \vdots & \vdots & \vdots & \ddots & \vdots \\ 0 & 0 & \cdots & \Delta_1^{\mathrm{T}} & 0 & 0 & \cdots & \Delta_k^{\mathrm{T}} & 0 & 0 & \cdots & \Delta_P^{\mathrm{T}} \end{bmatrix}^{\mathrm{T}_b},$$ (5)

where the superscripted T_b is the block transpose operator. The matrix Δ is of size P blocks, where P is the total number of time samples. Each subbloc is of size $M \times (M \times N)$ where M is the total number of points along the span and N is the total number of modes. The total size of the matrix is $PM \times MN$ which represents $2PM^2N$ coefficients if we take into account the complex numbers storage for real and imaginary parts. This system of equations is overdetermined if $P > 2N$ and must be solved in a least-squares sense. Once, we have solved the system and obtained $\phi_{n_{\mathscr{R}e}}(z_j)$ and $\phi_{n_{\mathscr{I}m}}(z_j)$ for each n and each j in the domain, we compute the modal amplitude and the phase angle contribution:

$$|\phi_n(z_j)| = \sqrt{\phi^2_{n_{\mathscr{R}e}}(z_j) + \phi^2_{n_{\mathscr{I}m}}(z_j)} \quad \text{and} \quad \theta_n(z_j) = \tan^{-1}\frac{\phi_{n_{\mathscr{I}m}}(z_j)}{\phi_{n_{\mathscr{R}e}}(z_j)}.$$ (6)

The response can be easily reconstructed as the real part of the summation of n multiple waves as follows:

$$y(t_k, z_j) = \mathscr{R}e\left\{\sum_{n=1}^{N} |\phi_n(z_j)|e^{i(\omega_n t_k + \theta_n(z_j))}\right\}.$$ (7)

For each temporal mode n the corresponding wave form has a total phase $\omega_n t_k + \theta_n(z_j)$ that varies from point to point along the structure. If the dependence of the function θ to the space variable z is linear, i.e. $\theta_n(z) = k_n z$, then one can easily compute the phase velocity magnitude $C_n = \omega_n/k_n$ for each mode n. The term k_n represents a wavenumber and its sign the direction of travel.

This method can be assimilated to a double discrete fourier transform (DFT) and the amplitude $|\phi_n(z_j)|$ to a measure of the square-root of the power spectrum of the signal. In the following, we will apply the method to sets of dense spatio-temporal data obtained from DNS.

3. Simulation parameters and structure model

We consider the cases of the coupled interaction between a shear inflow and a flexible cylinder of aspect ratio $L/D = 2028$. The type of structure that is considered is a flexible cylinder under constant tension T, possessing non-negligible constant bending stiffness EI and only allowed to oscillate due to VIV in the cross-flow direction. The structure is pinned and hinged at both ends. The nondimensional equation of motion, based on a reference length D (cylinder diameter) and a reference velocity U (maximum inflow velocity), that is numerically solved is

$$\ddot{y} - \omega_c^2 \frac{\partial^2 y}{\partial z^2} + \omega_b^2 \frac{\partial^4 y}{\partial z^4} = \frac{1}{2}\frac{C_{\text{Lift}}}{m},$$ (8)

where $\omega_c = (T/\rho_s U^2)^{1/2}$ and $\omega_b = (EI/\rho_s U^2 D^2)^{1/2}$ are the nondimensional cable phase velocity and the beam phase velocity, respectively; ρ_s is the structural linear density. The forcing involves the nondimensional lift coefficient C_{Lift} computed iteratively by the three-dimensional flow solver.

The corresponding eigenspectrum *in vacuum* of that beam-cable structure is expressed as a function of the wavenumber k:

$$\omega^2 = \omega_b^2 k^4 + \omega_c^2 k^2, \quad k = \frac{n\pi}{(L/D)}.$$ (9)

The natural frequencies are here non-dimensional quantities. Here, n represents the nth spatial sine Fourier mode ($\sin(n\pi z/L)$) of the structure. In the following, we will refer to it as n_z. The phase velocity C is defined in this case as

$$C = \omega/k = \sqrt{\omega_b^2 k^2 + \omega_c^2} = \sqrt{\omega_{b^2}\left(\frac{n_z \pi}{L/D}\right)^2 + \omega_c^2}. \tag{10}$$

For all examples worked in this paper, the mass ratio of the structure is $m = \rho_s/\rho_f D^2 = 2$, the cable phase velocity is $\omega_c = 35$, the beam phase velocity is $\omega_b = 450$ (ρ_f is the fluid volumic density). The dimensional frequency values $\hat{f}_n$ may be computed with a proper scaling: $\hat{f}_n = (f_n U)/D$. The choice of including a priori the added mass coefficient in the computation of the natural frequencies of the structure is difficult because the added mass is not constant for different frequencies (Vandiver, 1993).

The excitation bandwidth and the extent of lock-in are strongly influenced by the type and the magnitude of the shear (Vandiver, 1993). These can be measured by the shear fraction $S_{fr} = \Delta U/U_{max}$ and the shear parameter $\beta = (D/L)S_{fr}$, which are nondimensional parameters. Moreover, if the excitation bandwidth includes the natural frequencies of more than one mode, a multi-moded response with no clear lock-in regions will most likely be dominant over the span. A measure of the likelihood of lock-in is the product between the excitation bandwidth and the modal density. The excitation bandwidth Δf, due to the sheared flow, can be estimated using a reduced velocity of approximately $U_r = 5.9$ and the variation in the velocity ΔU. The modal density of a constant tension cable is $1/f_1$, where $f_1 = \omega_1/2\pi$ is the first mode natural frequency obtained from Eq. (9). For a constant tension cable, the potential number of responding spatial modes referred to as N_z, can be approximated by $N_z = \Delta f/f_1 = \Delta U/(U_r f_1)$ where the different variables involved are non-dimensional quantities (Vandiver, 1993).

4. Results

The hydrodynamic loads in Eq. (8) are computed by a parallel three-dimensional Navier–Stokes solver, $\mathcal{N}\varepsilon\kappa\mathcal{T}\alpha r$, based on the spectral/$hp$ element method (Karniadakis and Sherwin, 1999) and used for various VIV applications (Lucor et al., 2001, 2003, 2005; Dong and Karniadakis, 2005). This version of the code employs a hybrid scheme utilizing Fourier collocation in the spanwise z-direction (cylinder axis) and Jacobi-Galerkin formulation on $(x–y)$-planes perpendicular to the cylinder axis. The spanwise Fourier decomposition offers a more flexible alternative to general full three-dimensional mesh/flow computation, and allows for a relatively low computational cost. In case of shear flows, the spanwise resolution becomes a critical issue (Lucor et al., 2003) and enough Fourier modes have to be used along this direction in order to capture the scale of the correlation length of the flow. Furthermore, the Fourier decomposition implies periodicity of the solution and of the imposed sheared velocity profile at the inflow. Therefore, there must exist a confined region or buffer region along the spanwise direction in which the velocity adjusts itself to satisfy periodicity (Lucor, 2004).

A 2-D hybrid grid of 1018 elements in the (x, y)-plane (Evangelinos and Karniadakis, 1999) with polynomial order $p = 8$ and 64 Fourier complex exponential modes in the z-direction (corresponding to a resolution of 128 collocation points) are used. The spatial resolution in the $(x–y)$-plane insures the presence of (at least) four computational nodes within the flow boundary layer developing at the wall at Re = 1000. This resolution is appropriate to resolve all the turbulent scales in the $(x–y)$-plane and the larger scales only along the z-direction. However, based on our experience and the study in (Lucor et al., 2003), we believe that this spanwise resolution is sufficient to accurately capture the response within a 15% error range at these moderate shear parameters and Reynolds numbers. The temporal resolution used in this study provides roughly 5000 time samples per period of oscillation. In this work, buffer region velocity profiles are represented by third-order polynomials (linear case) and exponential functions (exponential case) that insure continuity and periodicity of the velocity profile, its slope and its curvature. In agreement with Lucor et al. (2003), the length of the buffer region is kept lower than 10% of the total length of the structure.

We define the Reynolds number based on the maximum velocity of the incoming shear inflow that is always located at zero depth. In our study, we set it to be Re = 1000. First, we consider the case of a linearly sheared flow past a flexible cylinder; then the case of an exponentially sheared flow; both cases representing realistic situations corresponding to experimental and field conditions (Furnes, 1998).

4.1. Linear shear

In this case we obtain: $S_{fr} = \Delta U/U_{max} = 0.7$ and $\beta = (D/L)S_{fr} = 3.45 \times 10^{-4}$. A 70% variation in flow velocity is much larger than the approximately 25% maximum lock-in bandwidth which is suggested as an upper limit in Vandiver

(1993). The potential number of simultaneously responding modes is approximately $N_z = 14$. These results indicate that a multiple-mode response is likely.

In the following, the numerical data we present have been windowed using a Hanning window and zero padded prior to the modal decomposition in order to reach a spectral resolution $\Delta f_n = 0.125\%$. Fig. 1 shows the time-evolution of the cross-flow response along the span. The minimum inflow velocity is 30% of the maximum velocity and is located at maximum depth. The depth-axis is normalized by D. Fig. 2 shows the spanwise spectrum $|\phi_n(z_j)|$ versus frequencies, obtained from the phase reconstruction procedure described in Section 2. A total number of $N = 512$ modes (cf. Eq. (1)) are used in the decomposition in order to get a good resolution. Fig. 2(b) displays a close-up view. Fig. 3(a) shows the span-averaged values of the modal amplitude response. As seen in Lucor et al. (2003), the existence and magnitude of low modes in the response depend strongly on their presence in the initial conditions of the structure. When they exist in our simulations, those low modes seem to be sustained by the system for a long time, despite the lack of any hydrodynamic forcing at the corresponding frequencies. Therefore, we believe that low modes are most likely unphysical in this case and can be neglected (if they do exist, they do not contribute significantly to the fatigue of the material anyway). The graph exhibits three clear main peaks at $f = 0.182;\ 0.193;\ 0.204$. We note, however, that each of these three frequency peaks is dominant only over a portion of the span, with the highest frequency dominating close to
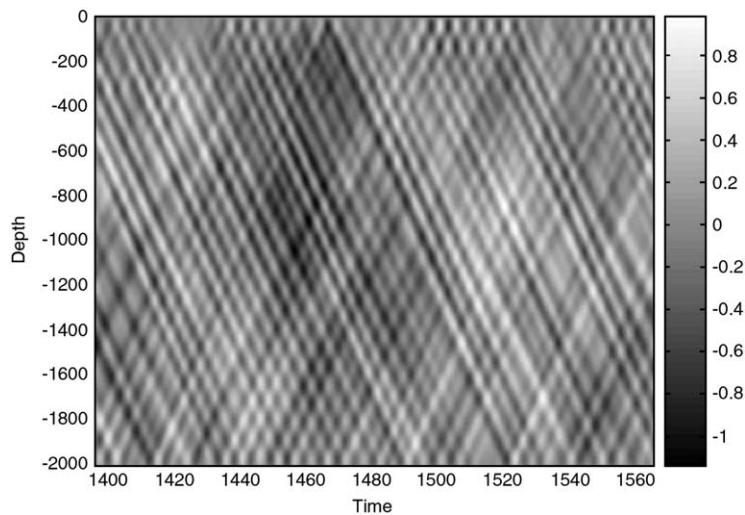

Fig. 1. Time-evolution of the spanwise distribution of the crossflow non-dimensional response $y(t, z)$ of the riser.
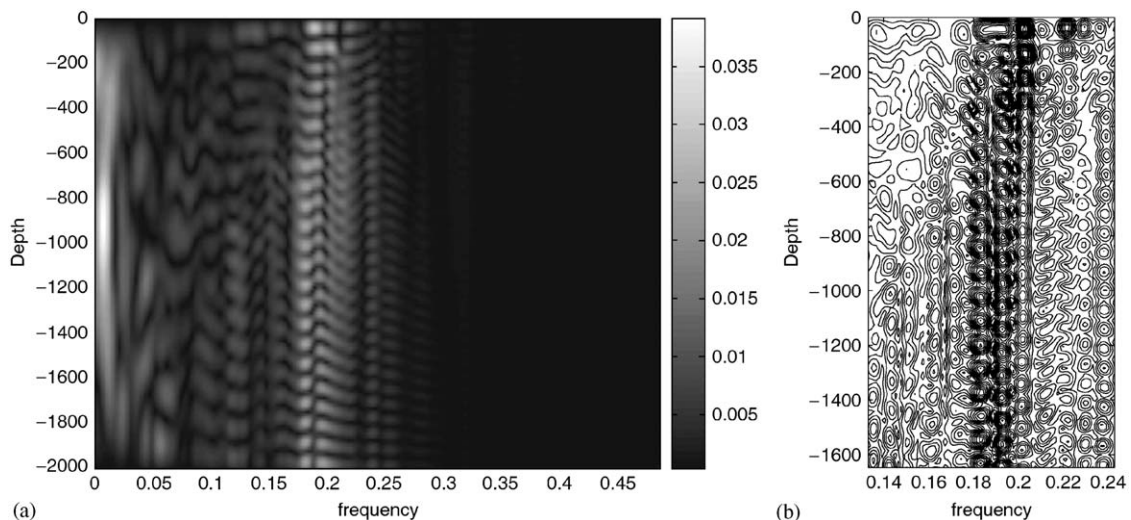

Fig. 2. (a) Spanwise distribution of the modal amplitude response $|\phi_n|$; (b) close-up of $|\phi_n|$ around the Strouhal frequency.
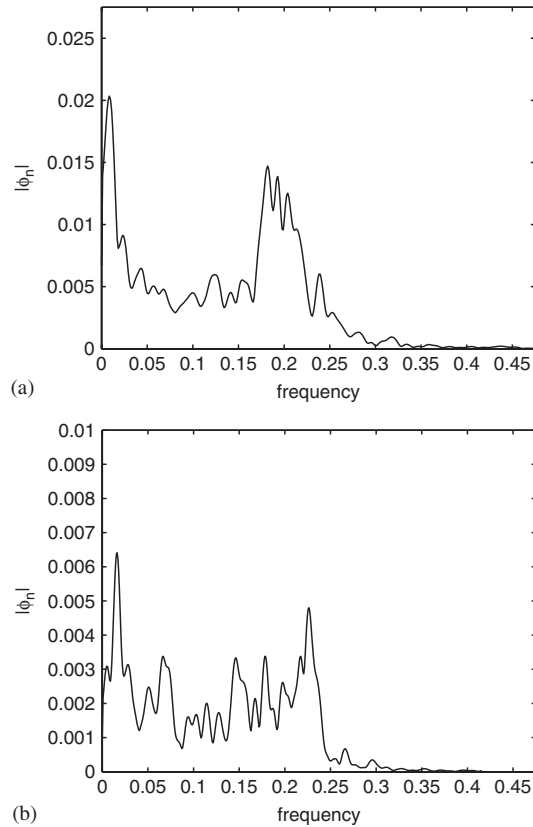
Fig. 3. Span-averaged distribution of the modal amplitude response $|\phi_n|$: (a) linear case; (b) exponential case.
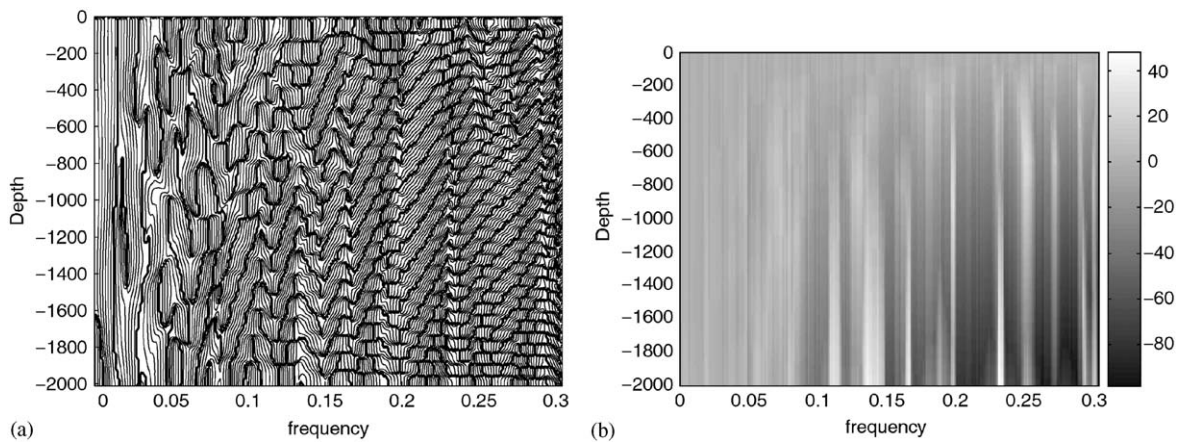

Fig. 4. Spanwise modal phase angle response θ_n: (a) wrapped phase angle; (b) unwrapped phase angle.

the surface, the medium frequency around the mid and low regions, and the lowest frequency along the bottom one-third of the span. This is clear on the iso-contour plot of Fig. 2(b) that shows a close-up of the modal amplitude distribution. We also note the emergence of the lower modes along the bottom half part of the cylinder. As one considers regions from top to bottom, the leading peak shifts from right to left in the spectrum. The energy is mainly distributed among the three leading frequencies.

Fig. 4 shows the modal phase angle $\theta_n(z_j)$ as a function of z, at all frequencies. Fig. 4(a) shows the distribution of the phase angle. As it exhibits discontinuities when the phase jumps at multiples of 2π, it is harder to interpret than the right plot that shows the unwrapped numerical values. We notice a region in the low frequency modes with almost no spanwise variation, corresponding to standing waves. For medium and high modes, there exists a dominant trend of linearly decreasing phase angle from top to bottom, demonstrating the existence of traveling waves from the surface to the bottom (cf. Eq. (7)). In few places we find an opposite gradient, which means that the traveling waves progresses in the opposite direction. In Fig. 4(a), we note that there exist groups of inclined bands defined by dark lines, that spread along the span-frequency plot; these dark lines represent phase jumps. These bands are almost parallel to the cylinder axis for the low modes, indicating standing waves in the physical space. The structures become slanted for higher modes with slopes that tend to 90° relative to the cylinder axis, indicating traveling waves with increasingly faster phase velocity.

We note two additional phenomena of interest: first, there are regions of strong reflections close to the domain boundaries, manifesting themselves as "cells" of rectangular shape; they are more apparent for high frequencies, and on the side of the low inflow velocity (maximum depth). Second, we note the presence of longitudinal discontinuities in the slopes of the band structures, particularly for frequencies around $f_n = 0.2$ and higher. This shows that the increase of the phase velocity versus frequency is not continuous, as modes travel in groups; one group travels at a certain speed, while the next group travels at a different speed.

Fig. 5 highlights the piecewise almost-linear behavior of the phase angle θ_n along the span, and the presence of reflection close to the boundaries. Fig. 5(a) shows the spanwise unwrapped phase angle at the three peak frequencies corresponding to Fig. 3(a). In Fig. 5(b) we present the corresponding slopes that form quasi-piecewise step functions. For a given mode n a constant positive slope indicates a wave traveling from top to bottom at constant speed. A negative sign indicates a wave progressing from bottom to top. We recall that the local slope of θ_n is the first-order approximation to the wavenumber k_n.

Fig. 6(a) shows the spanwise wavenumber k_n for all frequencies. Here, the amplitude of the contour plot indicates the wavenumber magnitude, while the sign only indicates the direction of traveling. We can identify three main regions: the dark regions, toward the low modes, correspond to standing waves; the light gray regions correspond to traveling waves moving from top (high inflow velocity) to bottom; and the medium gray regions correspond to traveling waves moving from bottom to top.

Fig. 6(b) shows the corresponding excited spatial sine Fourier modes equal to $(k_n(z_j)L)/\pi D$.

A short study (not presented here) showed the existence of a correlation between the magnitude of the modal phase amplitude $|\phi_n|$ and the modal phase angle θ_n. Indeed, a comparison between the span-averaged distribution of the modal phase angle slopes and the span-averaged distribution of the modal amplitude, away from the regions of strong
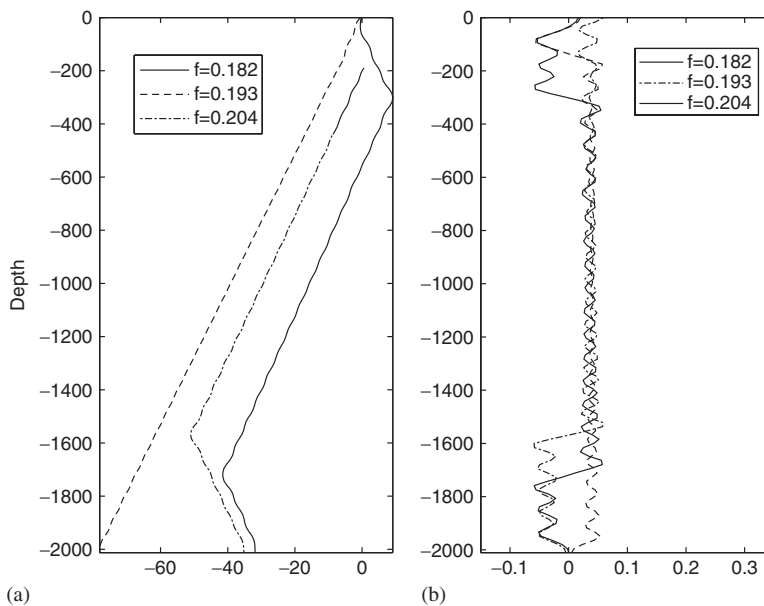

Fig. 5. (a) Spanwise unwrapped phase angle $\theta_n(z_j)$ at three different frequencies; (b) corresponding spanwise wavenumber k_n.
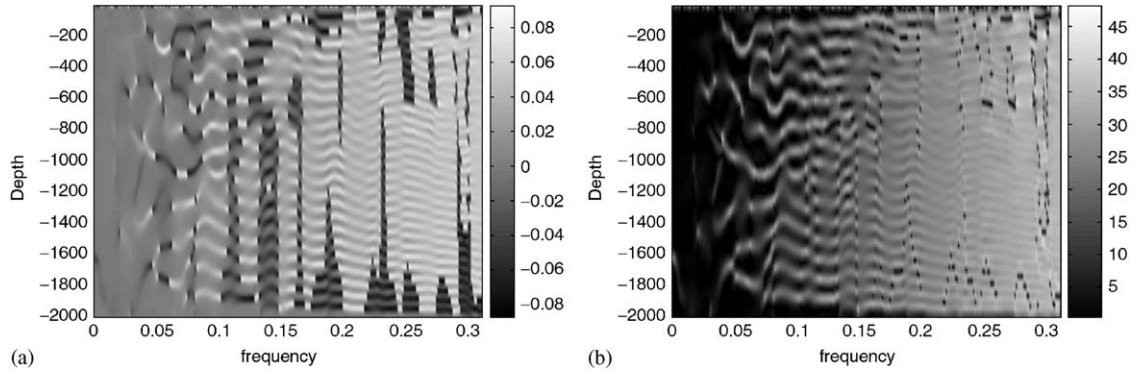
Fig. 6. (a) Spanwise wavenumber k_n of the riser at all frequencies; (b) spanwise distribution of the spatial sine Fourier mode at all frequencies.
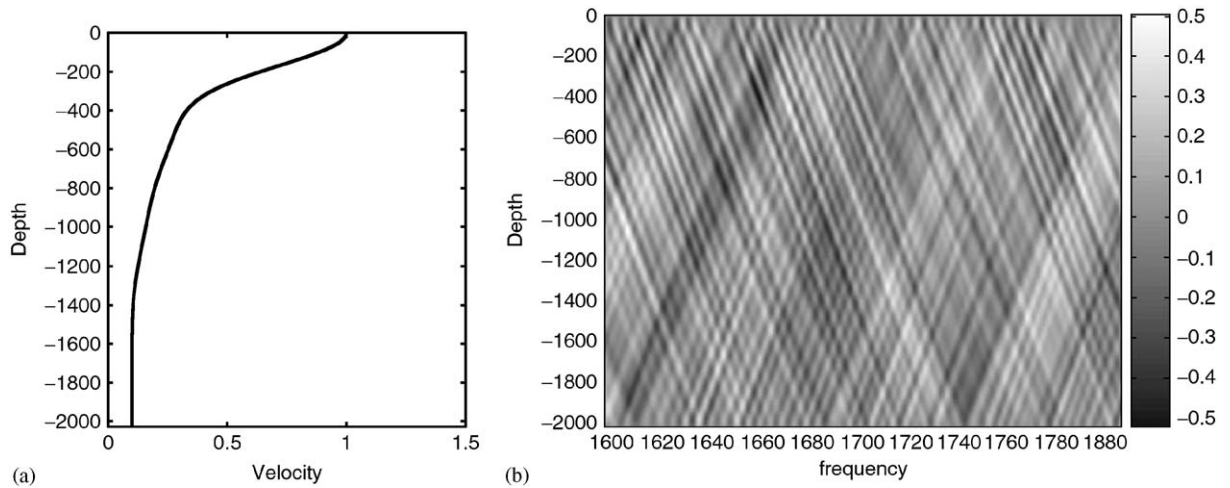

Fig. 7. (a) Inflow velocity profile for the exponential case; (b) corresponding time-evolution of the crossflow non-dimensional response $y(t, z)$ of the riser.

reflections, indicated a strong correlation between the two quantities. We noticed in particular that the two curves synchronized well: troughs in the latter correspond to notches in the former, while maxima in the spectrum coincide with the centers of (almost) linearly increasing regions. We recall that notches in the slopes of the phase angle correspond to reflecting waves, traveling from bottom to top.

4.2. Exponential shear

Exponentially sheared profiles represent more realistic configurations for marine engineering applications. The shear fraction and shear parameter are important parameters; as well as the shape of the inflow profile, in particular how fast the velocity distribution drops along the span of the structure. Fig. 7(a) shows the inflow velocity as function of the span. The shear fraction is $S_{fr} = \Delta U / U_{max} = 0.9$ and β depends on the value of the slope. We can define it as: $\beta = (D/\bar{U})(\overline{\partial U(z)/\partial z})$; hence, using averaged values, $\beta \approx 1.75 \times 10^{-3}$. Again the variation in flow velocity is large and the number of potentially responding modes is approximately $N_z = 18$, indicating a probable multi-frequency response. Again, the numerical data we present have been windowed using a Hanning window and zero-padded prior to the modal decomposition. A total number of $N = 512$ modes (cf. Eq. (1)) are used in the decomposition. Fig. 7 shows the time-evolution of the cross-flow response across the span. The maximum inflow velocity occurs at zero depth and the minimum inflow velocity, equal to 10% of maximum, at maximum depth. Fig. 8(a) shows the spanwise spectrum
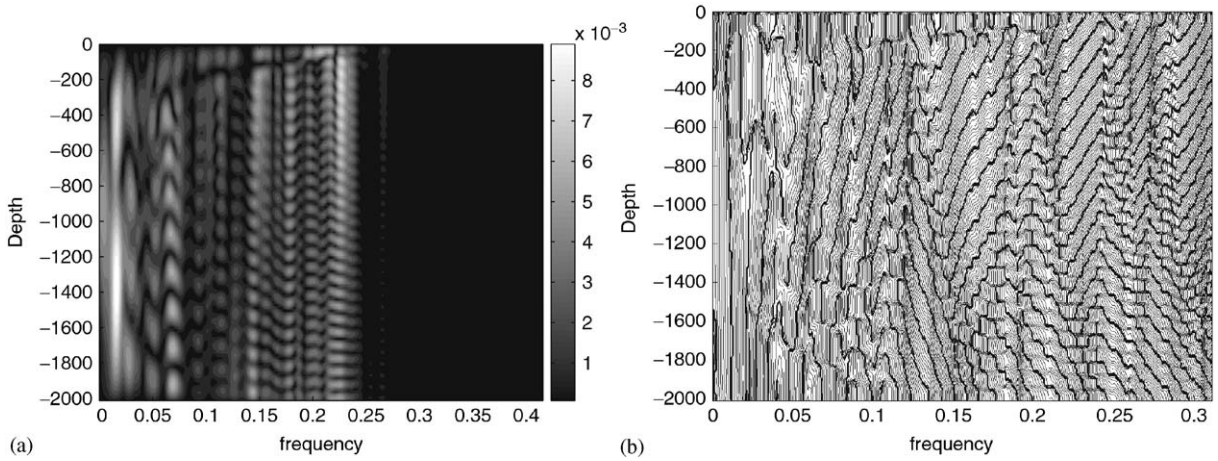
Fig. 8. (a) Spanwise modal amplitude $|\phi_n|$; (b) phase angle response θ_n.

$|\phi_n(z_j)|$, obtained from the phase reconstruction procedure, after Hanning windowing and zero-padding of the original data. Fig. 3(b) shows the span-averaged values of the modal amplitude response. There are more peaks than in the linear case and the total energy is spread out over many frequencies. We notice some relatively low frequencies in the [0.05; 0.1] range that are excited and capture a significant part of the energy in particular on the side of the low inflow incoming velocity. These low modes have to be distinguished from the very low modes which are most likely unphysical (Lucor et al., 2003). Fig. 8(b) reveals more pronounced reflection waves than in the linear case and the traveling waves do not reach the bottom. This is probably due to the almost constant-velocity region close to the bottom (cf. Fig. 7(a)). The energy injected by the current at the surface is distributed and propagated over some distance down the surface, but the shear is not strong enough to carry it to the ocean floor. Fig. 9 shows a piecewise almost-linear change of the phase angle θ_n along the span, showing reflections close to the boundaries. Fig. 9(a) shows the spanwise unwrapped phase angle at the three highest peak frequencies corresponding to the right plot of Fig. 3(b). In Fig. 9(b), we show the corresponding slopes that form quasi-piecewise-step functions. For a given mode n, a constant positive slope indicates a traveling wave from top to bottom, while a negative sign indicates that the wave progresses from bottom to top. The difference with the linear case is that the phase velocity of the three traveling waves are different and their magnitude increases with increasing frequency.

4.3. Low-order model

The modal decomposition proposed here is intended to shed some light on the principal mechanisms of flow-structure energy transfer. A full decomposition of the data is not tractable because it requires too many modes. We propose to simplify the decomposition by considering only the most energetic modes, in the form of clustered packets of adjacent modal responses near a spectral peak. The success of this decomposition is judged on the basis of how closely the sum of these selected modes represents the total response. The statistical measure of the approximation is: the root mean square (r.m.s.) value of the response $y_{\mathrm{r.m.s.}}$ at each location z_j along the cylinder, which is related to the energy distribution of the response. We define

$$y_{\mathrm{r.m.s}}(z_j) = \left\{ \frac{1}{P} \sum_{k=1}^{P} (y(t_k, z_j) - \bar{y}(z_j))^2 \right\}^{1/2}, \tag{11}$$

where $\bar{y}(z_j)$ is the mean value in time, and P is the total number of time samples; the full decomposition of the response being given in Eq. (7). Due to the orthogonality of the DFT basis, the r.m.s. fluctuations can be directly expressed as a function of the modal amplitude coefficients, such that we have

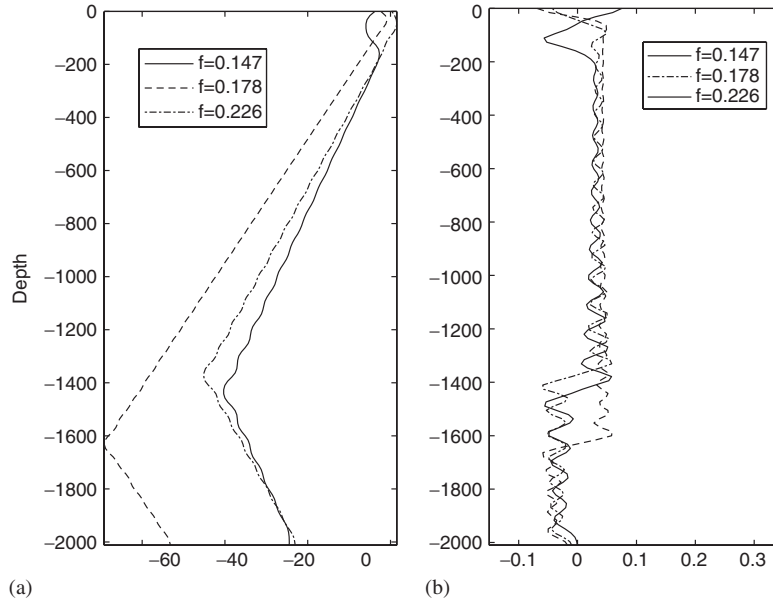$$y_{\mathrm{r.m.s.}}(z_j) = \left\{ \sum_{n=1}^{N} \frac{1}{2} |\phi_n(z_j)|^2 \right\}^{1/2}. \tag{12}$$

Fig. 9. (a) Spanwise (unwrapped) phase angle $\theta_n(z_j)$ at three different frequencies; (b) corresponding spanwise wavenumber k_n.

The summation starts here with the second mode in order to exclude the mean value. For a low-order model, the approximated response $\hat{y}$ is represented with a smaller number of modes $N_s < N$ which forms a subset of the original space. The new representation and corresponding fluctuations read

$$\hat{y}(t_k, z_j) = \mathcal{R}e\left\{\sum_{n=1}^{N_s} |\phi_n(z_j)| e^{i(\omega_n t_k + \theta_n(z_j))}\right\} \quad \text{and} \quad \hat{y}_{\text{r.m.s.}}(z_j) = \left\{\sum_{n=1}^{N_s} \frac{1}{2}|\phi_n(z_j)|^2\right\}^{1/2}. \tag{13}$$

If the total energy in the system was exactly distributed among a finite number of discrete frequencies and the signal was infinitely repeatable, the spectrum of the response would be zero everywhere except at those frequencies, and these modes would be sufficient to compute exactly the r.m.s. values. However, the brevity of the original signal, combined with the frequency variability of the excitation, lead to spectral leakage of the energy into neighboring frequencies, forming lobes of various widths. Hence, there is a numerical as well as a physical reason for the existence of those clusters of modes in the frequency domain. The variability of the excitation force, caused by such factors as the shear fraction, shear parameter, inflow profile shape, Reynolds number, and turbulence level; and the structural properties, such as mass ratio, damping factor, aspect ratio, control the width of those lobes, which vary with frequency and along the span. We first decompose the frequency domain into an arbitrary number Q of subdomains, not necessarily contiguous or equal in length, based on the location and magnitude of peaks in the modal amplitude spectrum (cf. Fig. 10). Each domain b is located around a local maximum and is itself divided into two subdomains b^- and b^+ on each side of the local frequency peak. The subdomains are therefore equal in number to the Q selected maxima. This procedure and, in particular, the search of those points and indexing of the subdomains is repeated for each spanwise location z_j. We write

$$\hat{y}_{\text{r.m.s.}}(z_j) = \left\{\sum_{b=1}^{Q} \Phi_b(z_j)\right\}^{1/2} \quad \text{with} \quad \Phi_b(z_j) = \sum_{n=h_b(-1)}^{h_b(1)} \frac{1}{2}|\phi_n(z_j)|^2. \tag{14}$$

Here the function h_b maps the frequency interval b under consideration to a reference $[-1; 1]$ interval. Therefore, the $h_b(-1)$ value corresponds to the lower bound of the frequency interval; and $h_b(1)$ to the upper bound. The upper point is excluded in the summation of the next interval to avoid counting it twice.
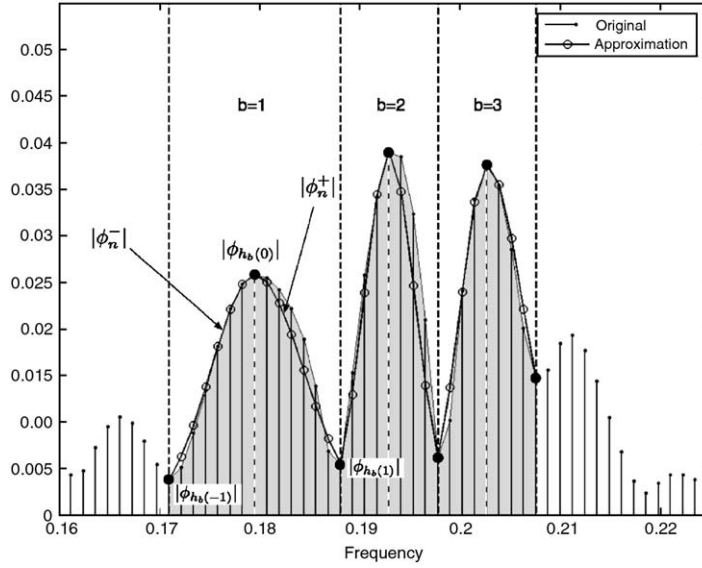
Fig. 10. Schematic of the domain decomposition and modal amplitude reconstruction at a specific z_j location. In this example, the number of subdomains is $Q = 3$. Each subdomain b is split into two parts, one on each side of a selected frequency peak. Small black dots at the edge of the shaded area represent the target spectrum. Open circles represent the reconstructed Gaussian-shaped spectrum.

We decompose the previous relation as

$$\Phi_b(z_j) = \sum_{n=h_b(-1)}^{h_b(0)-1} \frac{1}{2}|\phi_n^-(z_j)|^2 + \sum_{n=h_b(0)}^{h_b(1)} \frac{1}{2}|\phi_n^+(z_j)|^2. \tag{15}$$

The modal distribution on each subdomain is approximated by a Gaussian function with a free parameter σ which is adjusted to fit the data. The choice of a Gaussian-type approximation of the lobe shape is arbitrary, but proved to be well adapted to the particular problem we study. The final expression is

$$\hat{y}_{\text{r.m.s.}}(z_j) = \left\{ \sum_{b=1}^{Q} |\phi_{h_b(0)}| \left[\sum_{n=h_b(-1)}^{h_b(0)-1} e^{-(1/2)((n-h_b(0))/P\sigma_b^-)^2} + \sum_{n=h_b(0)}^{h_b(1)} e^{-(1/2)((n-h_b(0))/P\sigma_b^+)^2} \right] \right\}^{1/2}, \tag{16}$$

with σ_b^- and σ_b^+ being defined as follows:

$$\sigma_b^- = \left\{ \frac{(h_b(-1) - h_b(0))^2}{2P^2 \log(|\phi_{h_b(0)}|/|\phi_{h_b(-1)}|)} \right\}^{1/2} \quad \text{and} \quad \sigma_b^+ = \left\{ \frac{(h_b(1) - h_b(0))^2}{2P^2 \log(|\phi_{h_b(0)}|/|\phi_{h_b(1)}|)} \right\}^{1/2}. \tag{17}$$

The numerical procedure is applied to the linear and the exponential cases. Fig. 11 compares the r.m.s. spanwise distribution values of the original response and the approximated response for different number of lobes Q. Fig. 11(a) shows results for the linear case, while Fig. 11(b) shows results for the exponential case. We see that the r.m.s. values of the approximated response converge to the r.m.s. values of the original response as we increase Q. We also notice than the r.m.s. values are larger on the side of the high inflow velocity (close to the surface) for the exponential case, but not for the linear case. Moreover, standing wave solutions are more apparent in the linear profile case, particularly close to the domain boundaries, than for the exponential profile case. Fig. 11(c) shows the percent error $\varepsilon = \left(\sum_{j=1}^{M} \hat{y}_{\text{r.m.s.}}(z_j) / \sum_{j=1}^{M} y_{\text{r.m.s.}}(z_j) \right)^{1/2}$ of the r.m.s. values versus the total number of subdomains Q for the linear and the exponential cases. The rate of convergence is a nonlinear function of Q; less modes are necessary to reach the same level of accuracy in the linear case than in the exponential case, as expected. For the linear case, only three subdomains ($Q = 3$), equivalent to knowing seven discrete modal amplitudes (cf. Fig. 10), are enough to recover more than 75% of the energy. For the exponential case, 13 spectral values are required to reach the same approximation.
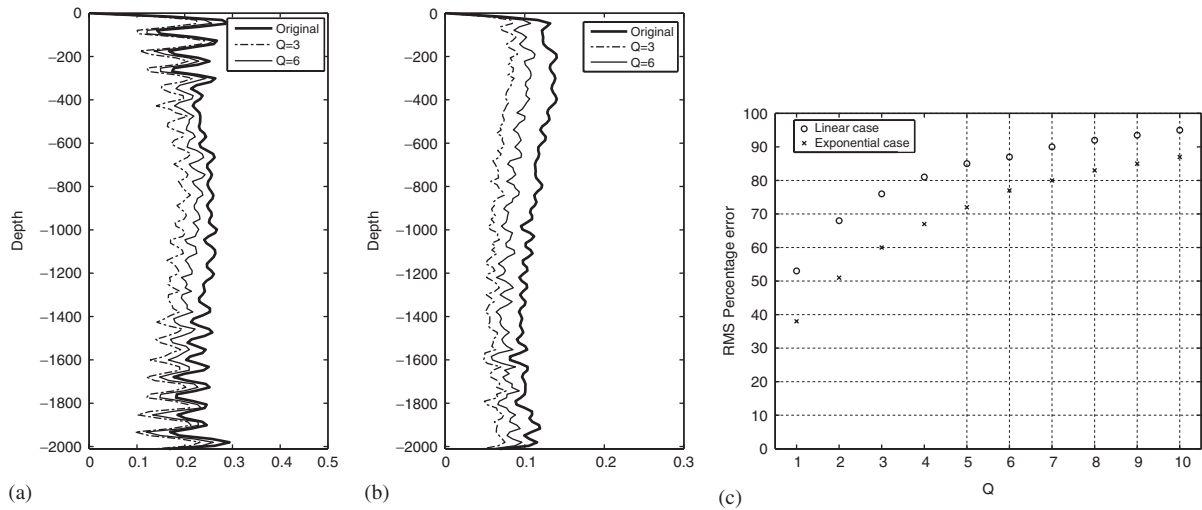
Fig. 11. Spanwise distribution of the original and approximated responses as function of the number of subdomains Q used: (a) linear case, (b) exponential case, (c) Convergence of the r.m.s. values versus the number of subdomains Q for the linear and the exponential cases.

5. Conclusions

We have developed a systematic methodology to extract the VIV modes of a riser, based on data from CFD coupled to a long ($L/D \approx 2000$) tensioned beam placed transversely to (a) a linearly sheared flow, and (b) an exponentially sheared flow. The "modes" we estimate are in fact nonlinear equilibria between the flow-induced excitation forces and the structural dynamics.

A principal feature of riser modes is that they are *complex modes* possessing varying amplitude and phase at each point of the riser, and cannot be described by standing waves. For higher frequencies and for both the linear and exponential shear, the mid-span of the beam shows mainly traveling waves from top (high velocity) to bottom, while the ends contain reflections due to the boundary conditions. Low frequency modes are largely standing waves.

We have developed simplifying procedures to represent the VIV response in terms of a few clusters of modes, which nonetheless capture the essence of the response.

References

Dong, S., Karniadakis, G., 2005. DNS of flow past a stationary and oscillating cylinder at Re = 10 000. Journal of Fluids and Structures 20, 519–531.

Evangelinos, C., Karniadakis, G., 1999. Dynamics and flow structures in the turbulent wake of rigid and flexible cylinders subject to vortex-induced vibrations. Journal of Fluid Mechanics 400, 91–124.

Furnes, G., July 1998. On marine riser responses in time and depth dependent flows. Technical Report, Norsk Hydro, Bergen, Norway.

Gopalkrishnan, R., Grosenbaugh, M., Triantafyllou, M., 1992. Amplitude modulated cylinders in constant flow: Fundamental experiments to predict response in shear flow. In: Third International Symposium on Flow Induced Vibrations and Noise. ASME, Anaheim California.

Govardhan, R., Williamson, C., 2000. Modes of vortex formation and frequency response of a freely vibrating cylinder. Journal of Fluid Mechanics 420, 85–130.

Karniadakis, G., Sherwin, S., 1999. Spectral/hp Element Methods for CFD. Oxford University Press, Oxford.

Lucor, D., 2004. Generalized polynomial chaos: applications to random oscillators and flow–structure interactions. Ph.D. Thesis, Brown University.

Lucor, D., Imas, L., Karniadakis, G., 2001. Vortex dislocations and force distribution of long flexible cylinders subjected to sheared flows. Journal of Fluids and Structures 15, 641–650.

Lucor, D., Ma, X., Triantafyllou, M., Karniadakis, G., 2003. Vortex-induced vibrations of long marine risers in sheared flows. In: Proceedings of the 4th ASME/JSME Joint Fluids Engineering Conference, 6–10 July 2003, Honolulu, Hawaii, USA.

Lucor, D., Foo, J., Karniadakis, G., 2005. Vortex mode selection of a rigid cylinder subject to VIV at low mass-damping. Journal of Fluids and Structures 20, 483–503.

Sarpkaya, T., 1979. Vortex-induced oscillations. Journal of Applied Mechanics ASME 46, 241–257.

Stansby, P., 1976. The locking-on of vortex shedding due to cross stream vibration of circular cylinders in uniform and shear flows. Journal of Fluid Mechanics 74, 641.

Triantafyllou, M., Triantafyllou, G., Tein, D., Ambrose, B., 1999. Pragmatic riser VIV analysis. Offshore Technology Conference, Paper OTC 10931.

Triantafyllou, M., Hover, F., Techet, A., Yue, D., 2003. Vortex-induced vibrations of slender structures in shear flow. In: Benaroya, H., Wei, T. (Eds.), IUTAM Symposium on Integrated Modeling of Fully Coupled Fluid Structure Interactions Using Analysis, Computations and Experiments. Kluwer, Dordrecht.

Vandiver, J., 1993. Dimensionless parameters important to the prediction of vortex-induced vibrations of long, flexible cylinders in ocean currents. Journal of Fluids and Structures 7, 423–455.

Vandiver, J., Allen, D., Li, L., 1996. The occurence of lock-in under highly sheared conditions. Journal of Fluids and Structures 10, 555–561.

Zdravkovich, M., 1997. Flow around circular cylinders. Vols. 1 and 2. Oxford University Press, Oxford.